ACS APPLIED MATERIALS & INTERFACES

Research Article

www.acsami.org

Degradation of Methylene Blue Using Porous WO_3, SiO_2–WO_3, and Their Au-Loaded Analogs: Adsorption and Photocatalytic Studies

Daniel P. DePuccio,[†] Pablo Botella,[‡] Bruce O'Rourke,[†] and Christopher C. Landry*[,†]

[†]Department of Chemistry, University of Vermont, 82 University Place, Burlington, Vermont 05405, United States

[‡]Instituto de Tecnología Química, UPV-CSIC, Avenida de los Naranjos s/n, Valencia 46022, Spain

Supporting Information

ABSTRACT: A facile sonochemical approach was used to deposit 3–5 nm monodisperse gold nanoparticles on porous SiO_2–WO_3 composite spheres, as confirmed by powder X-ray diffraction (XRD) and transmission electron microscopy (TEM). High-resolution TEM (HR-TEM) and energy dispersive X-ray spectroscopy (EDS) further characterized the supported Au nanoparticles within the Au–SiO_2–WO_3 composite. These analyses showed isolated Au nanoparticles within both SiO_2- and WO_3-containing regions. Selective etching of the SiO_2 matrix from Au–SiO_2–WO_3 yielded a pure Au–WO_3 material with well-dispersed 10 nm Au nanoparticles and moderate porosity. This combined sonochemical-nanocasting technique has not been previously used to synthesize Au–WO_3 photocatalysts. Methylene blue (MB) served as a probe for the adsorption capacity and visible light photocatalytic activity of these WO_3-containing catalysts. Extensive MB demethylation (azures A, B, C, and thionine) and polymerization of these products occurred over WO_3 under dark conditions, as confirmed by electrospray ionization mass spectrometry (ESI-MS). Photoirradiation of these suspensions led to further degradation primarily through demethylation and polymerization pathways, regardless of the presence of Au nanoparticles. Ring-opening sulfur oxidation to the sulfone was a secondary photocatalytic pathway. According to UV–vis spectroscopy, pure WO_3 materials showed superior MB adsorption compared to SiO_2–WO_3 composites. Compared to their respective nonloaded catalysts, Au–SiO_2–WO_3 and Au–WO_3 catalysts exhibited enhanced visible light photocatalytic activity toward the degradation of MB. Specifically, the rates of MB degradation over Au–WO_3 and Au–SiO_2–WO_3 during 300 min of irradiation were faster than those over their nonloaded counterparts (WO_3 and SiO_2–WO_3). These studies highlight the ability of Au–WO_3 to serve as an excellent adsorbant and photodegradation catalyst toward MB.

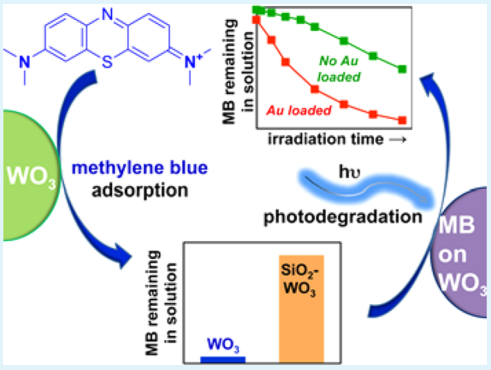

KEYWORDS: *gold nanoparticles, tungsten oxide, photocatalyst, sonochemical, demethylation*

INTRODUCTION

Tungsten oxide (WO_3) is an *n*-type semiconductor that has been extensively studied for applications in gas sensing, catalysis, solar energy conversion, and electrochromic displays.[1−6] With a small band gap of 2.4–2.8 eV, WO_3 is more effective than TiO_2 at absorbing visible light. Indeed, WO_3 has been studied as a visible light photocatalyst.[7,8] It is resistant to degradation due to photocorrosion,[9] which can lead to the formation of metal ions and decrease catalytic activity. Importantly, a deep lying valence band (+3.1 eV) favors oxidation reactions on the WO_3 surface.[9,10] These attributes make WO_3 a promising alternative to TiO_2, which needs to be modified in order to absorb visible light.

In addition to favorable photocatalytic attributes, WO_3 surfaces possess highly negative surface charges that are ideal for adsorption applications, especially for cationic dyes such as methylene blue (MB). Negative charges on the surface of WO_3 are a result of the oxide's low isoelectric point (IEP = 0.2–1). Studies using other WO_3 nanostructures have also taken advantage of this strong electrostatic interaction between MB and WO_3.[11−13] The combination of high adsorption capacity for MB and the photocatalytic nature of the WO_3 surface makes this oxide a strong candidate for subsequent conversion of adsorbed MB in aqueous systems.

Modifying WO_3 with Au nanoparticles has proven to be beneficial in improving the gas sensing,[14−16] photochromic, and electrochromic[17,18] properties of the pure oxide. Since Haruta's definitive review of catalysis performed by supported gold nanoparticles,[19] numerous studies have been conducted to further study and optimize these systems in various chemical transformations.[20,21] More recently, Au nanoparticles have been explored in photocatalysis applications,[22] with Au/TiO_2 being one of the most frequently studied systems.[23−26] The preparation and application of Au-loaded WO_3 visible light photocatalysts have not been thoroughly explored, however. It is expected that Au nanoparticles will facilitate better photocatalytic activity on the surface of WO_3 compared to pure WO_3. Enhancement of photocatalytic activity has been

Received: November 7, 2014
Accepted: December 30, 2014
Published: December 30, 2014

DOI: 10.1021/am507806a
ACS Appl. Mater. Interfaces 2015, 7, 1987–1996

demonstrated with different Au−WO_3 systems.[27−30] The increased photocatalytic ability of Au−WO_3 originates from the trapping of excited conduction band electrons in WO_3 by Au nanoparticles and increased e^-/h^+ (exciton) separation. Valence band holes (h^+) of WO_3 can be used for the oxidation of adsorbed molecules.[9,31−33] Alternatively, h^+ can oxidize surface H_2O to form reactive ·OH, which can subsequently oxidize adsorbed organics.[28] Improving the exciton separation on the WO_3 surface with Au nanoparticles will ultimately enhance photoreactivity toward adsorbed molecules.

Synthetically, there is still a great need for a facile and reliable method to deposit well-dispersed Au nanoparticles on the surface of WO_3. Due to the low IEP of WO_3, the simple deposition−precipitation (DP) technique is generally poor in creating small Au nanoparticles on this oxide and others that possess an IEP < 5.[34−37] Furthermore, physical methods to deposit Au nanoparticles on WO_3 such as pulsed laser deposition (PLD),[14] magnetron sputtering,[28,30,37] and aerosol assisted chemical vapor deposition (AACVD)[16,38] include expensive instrumentation, evacuated environments, and are not readily accessible in most laboratories.

Sonochemical deposition serves as a promising chemical route to overcome these shortcomings in order to easily prepare small Au nanoparticles on metal oxides. Previous work by Chen[39,40] and Gedanken[41] demonstrated the effectiveness of this method in the deposition of small (<5 nm) Au nanoparticles on silica. Most recently, Lin and co-workers[42] have used the sonochemical approach to deposit Au nanoparticles on the (001) and (101) facets of anatase TiO_2 to facilitate the plasmon-induced photocatalytic degradation of 2,4-dichlorophenol under visible light. The Au nanoparticles in that study possessed a mean diameter of 10−11 nm, but the thermal stability of the nanoparticles and the surface areas of the catalysts were not assessed. We predict that a porous SiO_2−WO_3 composite will serve as a suitable substrate for the sonochemical deposition of small Au nanoparticles, which will increase the visible light photocatalytic activity of these porous powders.

In the studies described here, a sonochemical approach is developed to deposit Au nanoparticles within the pores of acid-prepared mesoporous spheres (APMS) of silica previously impregnated with crystalline WO_3 (SiO_2−WO_3) to form Au−SiO_2−WO_3. Similar to the nanocasting technique, Au−SiO_2−WO_3 is selectively etched to form porous Au−WO_3. Porous Au−WO_3 particles have not been thoroughly developed for photocatalytic applications. This facile method avoids the problem of large Au NP deposition on WO_3 when using the traditional DP method. To the best of our knowledge, this combination of sonochemical and nanocasting techniques has not been previously studied for the deposition of Au nanoparticles on metal oxides. Herein, the Au nanoparticles are deposited without an organic stabilizer such as polyvinylpyrrolidone (PVP), which can negatively affect the Au−WO_3 interactions upon removal.[28] Lastly, solutions containing methylene blue (MB) are used to probe both the adsorption capacity and the visible light photocatalytic activity of Au-loaded and nonloaded oxides, and mass spectrometry is used to study the mechanism of MB photocatalytic conversion.

RESULTS AND DISCUSSION

Synthesis and Characterization of Materials. Mesoporous WO_3 and SiO_2−WO_3 microparticles with a spherical morphology were prepared as described in the Supporting Information. This process used a nanocasting procedure in which $(NH_4)_6H_2W_{12}O_{40}$, ammonium metatungstate or AMT, was impregnated into mesoporous silica spheres in several stages, followed by calcination at each stage to produce SiO_2−WO_3 microparticles with the same spherical morphology as the silica template. For some experiments, this material was etched with HF to dissolve the SiO_2, leaving pure WO_3 mesoporous microparticles with diameters of 1−3 μm, as confirmed by energy dispersive X-ray spectroscopy and scanning electron microscopy (Figure S1, Supporting Information). Purity of the WO_3 catalysts was further supported by elemental analysis (ICP-OES, see below).

Sonication of silica in aqueous solutions containing $HAuCl_4$ and NH_3, followed by calcination at 500 °C, has been shown to produce Au nanoparticles on the silica surface.[41] It is thought that the purpose of NH_3 is to activate silanol groups on the surface of SiO_2. Powerful jets formed during sonication then provide the necessary energy to propel Au species toward the SiO_2 surface, and upon impact, the Au reacts with free silanols or Si−O−Si species, resulting in the formation of Au−O−Si bonds. In previous research, the nature of Au−silanol bonds was indirectly characterized by Fourier transform infrared (FT-IR) measurements, which showed a disappearance of the isolated silanol stretching band when Au was deposited on the surface.[41] Here, this procedure was adapted for SiO_2−WO_3 to produce Au−SiO_2−WO_3. Although WO_3 dissolved to produce water-soluble tungstate ions (WO_4^{2-}) at the pH of the sonication (10.5),[43,44] we found that enough of the WO_3 remained to allow us to prepare Au−SiO_2−WO_3 by the sonication/calcination procedure with retention of the overall structural integrity of the nanocomposite. Attempts to use this sonication procedure on pure WO_3 to afford Au−WO_3 catalysts were unsuccessful. Excessive dissolution and degradation of WO_3 particles in the basic solution, as well as poor dispersion of Au nanoparticles, was observed when using pure WO_3 as the starting material. Therefore, SiO_2 in the initial substrate was necessary for successful Au deposition. Previous research suggested that sonication produces H· radicals in solution that reduce surface-bound Au^{3+} in $AuCl_4^-$ to Au^0.[41,42] In this study, however, the yellow color of the as-prepared samples before calcination indicated that Au^{3+} reduction did not occur in solution during sonication. After calcination of Au−SiO_2−WO_3, small, well-dispersed Au nanoparticles were found at low loadings, and the sample took on the characteristic red-purple color signifying Au reduction. This suggests that the main role of sonication in this synthesis is to facilitate bonding between the Au precursor and the SiO_2 surface. Finally, Au−WO_3 was then formed by removing the SiO_2 from Au−SiO_2−WO_3 by etching with HF. Elemental analysis confirmed complete removal of SiO_2 from both WO_3 and Au−WO_3. During the washing steps after this final HF treatment, the supernatant was dark purple after centrifugation. We attribute this to the loss of Au and smaller Au−WO_3 nanoparticles that are not retained on the spherical Au−WO_3 microparticles during etching. Indeed, the Au content of Au−WO_3 was less than Au−SiO_2−WO_3. The dark red-purple color of Au−WO_3 and further direct analyses indicated that crystalline Au nanoparticles remained on WO_3. A schematic summarizing the synthetic procedures is shown in Scheme 1.

The crystallinity of the materials was analyzed by powder X-ray diffraction (Figure 1). Mesoporous materials showed a broad peak at low angles due to pore-to-pore scattering. Materials containing WO_3 (composites and pure WO_3)

DOI: 10.1021/am507806a
ACS Appl. Mater. Interfaces 2015, 7, 1987−1996

Scheme 1. Summary of Synthesis Procedures Used to Prepare the Materials in These Experiments[a]

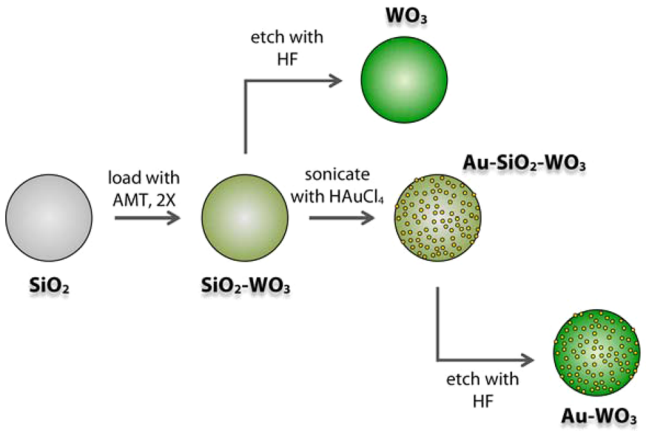

[a]"AMT" = ammonium metatungstate. Complete synthetic details are in the Supporting Information.

displayed high-angle diffraction peaks corresponding to monoclinic WO_3. All WO_3-containing samples exhibited peak broadening due to the nanocrystalline nature of the metal oxide. On the basis of Scherrer equation[45] calculations, nanoparticles of WO_3 ranged in sizes from 6 to 15 nm. These small WO_3 nanoparticles are aggregated and make up the spherical microparticles observed by SEM. It was clear that the sonochemical deposition of Au nanoparticles did not significantly alter the crystallinity of the WO_3. Au−SiO_2−WO_3 and Au−WO_3 showed an additional broad, weak intensity peak at 38° due to the Au(111) diffraction plane, which was used to estimate the crystallite diameter of the Au contained in those samples. X-ray diffraction data revealed Au nanoparticles with a diameter of 5 and 10 nm in Au−SiO_2−WO_3 and Au−WO_3, respectively. Transmission electron microscopy (TEM) was also used to characterize the nature of the deposited Au nanoparticles (Figure 1). Well-dispersed Au nanoparticles with diameters of 3−5 and 10 nm for Au−SiO_2−WO_3 and Au−WO_3, respectively, were confirmed by TEM. These nanoparticle sizes are in agreement with the XRD data. The presence of only larger (∼10 nm) Au nanoparticles in Au−WO_3 meant that the smallest nanoparticles are removed during the etching of the SiO_2 matrix.

The Au nanoparticles within Au−SiO_2−WO_3 were further characterized by EDS and high-resolution TEM (HR-TEM). A TEM image and corresponding EDS spectra at several locations within this region are shown in Figure 2. The EDS peak for Si (1.74 keV) is known to overlap with the adjacent W peak (1.78 keV), and in region 3 within this TEM image, the combined Si/W peak was clearly shifted to lower energies as compared to regions 1 and 2, signifying the presence of Si in region 3. Au was found both in areas containing pure WO_3 as well as those with combined SiO_2−WO_3. Thus, it appeared that the Au nanoparticles were in contact with all regions of the sample, not only those containing SiO_2. Figure 2 also shows a HR-TEM image of an isolated Au nanoparticle in contact with a WO_3 surface within the composite. Of note is the fact that this nanoparticle is slightly larger (∼10 nm) than the diameter calculated from XRD data (5 nm).

There is some evidence to suggest that the Au nanoparticles in contact with the WO_3 portions of the composite should be larger than those in contact with SiO_2, based on the difference in isoelectric point values of the two materials (WO_3 = 0.2−1; SiO_2 = 2). Another factor is the error associated with estimation of particle diameters from XRD data. However, it seems clear that the Au nanoparticles within Au−SiO_2−WO_3 were between 3 and 10 nm, depending on their location. In any case, the Au nanoparticles appeared to be uniformly deposited, hemispherical in shape, and highly crystalline. Measurements of the Au lattice fringes yielded a *d*-spacing of 0.23 nm, corresponding to the Au(111) plane, which is consistent with the XRD pattern. The measured *d*-spacing of 0.30 nm for the WO_3 corresponded to the (112) plane of monoclinic WO_3.

Sintering of Au nanoparticles is a common problem for catalysts during industrial catalytic reactions, as small Au nanoparticles tend to sinter at temperatures above 400 °C.[46−49] To observe the thermal stability of Au in our materials, Au−SiO_2−WO_3 was subjected to four heating cycles during which the samples were heated to 450 °C and held at that temperature for 3 h, cooling to room temperature between cycles. TEM showed that the particle size of the Au nanoparticles did not change significantly after this experiment (Figure S2, Supporting Information), indicating that the SiO_2−WO_3 composite is a good support for thermally stable Au nanoparticles.

The porosity of the materials was examined using N_2 physisorption (Table 1). The mesoporous silica substrate had only a moderate surface area (463 m^2 g^{-1}), consistent with its relatively large average pore diameter (78 Å). We found in previous studies that a large pore diameter was required for successful nanocasting that retained the particle morphology of the silica template. The surface areas of the SiO_2−WO_3 composite and the WO_3 product were consistent with a moderately porous material, given the increased mass of W relative to Si, and are also consistent with porous WO_3 from the

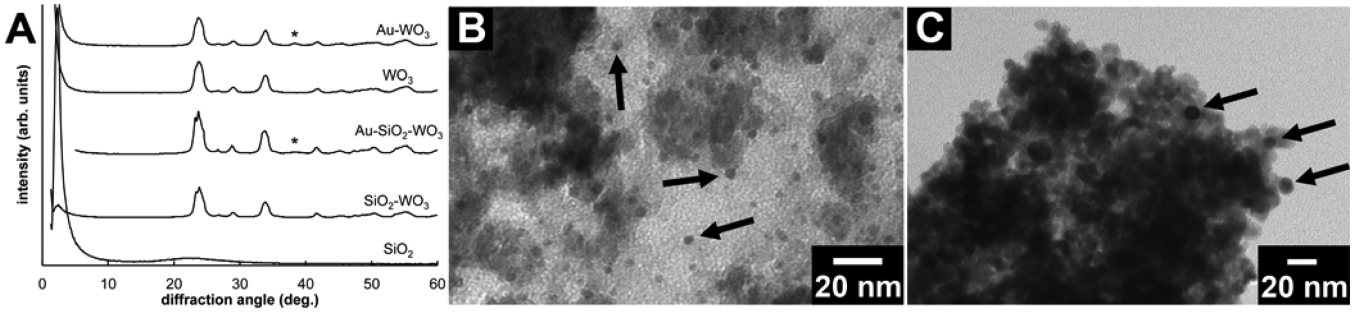

Figure 1. (A) Powder XRD patterns of materials prepared for catalytic experiments. The asterisk denotes the Au(111) peak. TEM images of (B) Au−SiO_2−WO_3 and (C) Au−WO_3. Arrows indicate Au nanoparticles.

DOI: 10.1021/am507806a
ACS Appl. Mater. Interfaces 2015, 7, 1987−1996

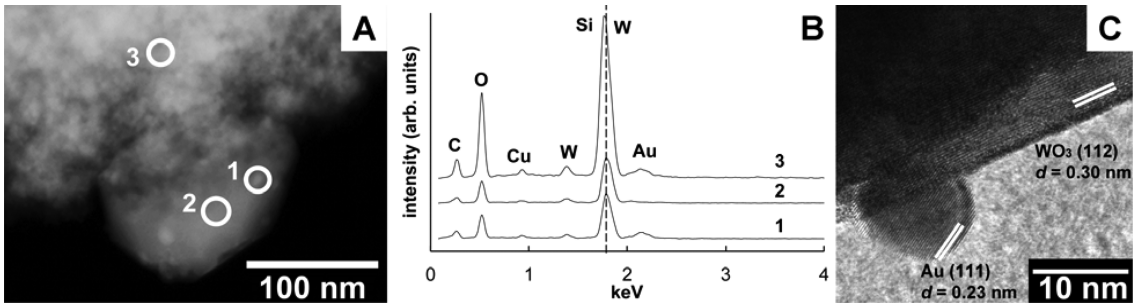

Figure 2. Structural characterization of Au−SiO_2−WO_3. (A) TEM image and (B) associated EDS of selected regions within Au−SiO_2−WO_3. Numbers in panel B correspond to sites identified in panel A. (C) HR-TEM image of an Au nanoparticle on an area of WO_3.

Table 1. Summary of Elemental Analysis, Au Nanoparticle Sizes, and N_2 Physisorption Data for the Porous Au-Loaded and Nonloaded Oxides Discussed in This Work[a]

sample	W (wt %)	Au (wt %)	Si/W (mole ratio)	W/Au (mole ratio)	Au diameter (nm)	SA_{BET} (m^2 g^{-1})	V_{pore} (cm^3 g^{-1})	d_{pore} (Å)
SiO_2						463	0.95	78
SiO_2−WO_3	49.1		1.15			65	0.12	47
WO_3	72.7		0.0033			53	0.20	101
Au−SiO_2−WO_3	51.3	0.40	1.27	137	3−5[b]	55	0.17	74
Au−WO_3	68.2	0.28	0.0054	261	~10[b]	66	0.24	135

[a]Weight percent and mole ratios determined by ICP-OES. [b]Measured by TEM and XRD.

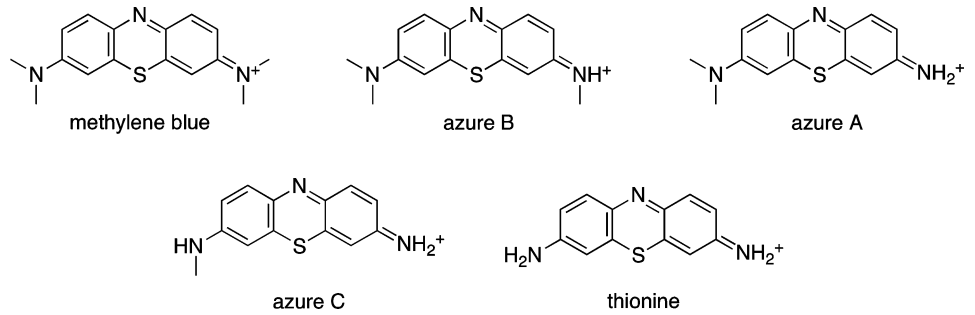

Figure 3. Methylene blue and the demethylated derivatives found by ESI-MS after adsorption and photocatalytic degradation.

literature. The decreased pore diameter of the SiO_2−WO_3 composite (47 Å) relative to the SiO_2 template showed that a significant portion of the SiO_2 pore surfaces had been modified with WO_3. Elemental analysis and the determined Si/W ratio of SiO_2−WO_3 showed that WO_3 was incorporated throughout the sample (Table 1). On the other hand, upon etching, the pore diameter increased significantly due to increased porosity of the material after removal of SiO_2. Importantly, the pure WO_3 sample had the same, if not slightly higher surface area than similar materials reported previously.[50,51]

Further changes in porosity were found for Au-loaded materials. While the surface area of Au−SiO_2−WO_3 decreased compared to SiO_2−WO_3, the pore diameter increased and was larger than expected based on the characterization of the SiO_2−WO_3 composite with no Au. This indicated that the pore surfaces had been modified during sonication and Au deposition and confirmed that some of the WO_3 dissolved in the basic aqueous solution used for sonication. It also showed that the effect of WO_3 dissolution and, to some extent, SiO_2 dissolution (pore expansion), played a greater role than Au nanoparticle deposition (pore blockage) in the resulting porosity of the Au−SiO_2−WO_3 composite. An increase in the Si/W mole ratio of Au−SiO_2−WO_3 in relation to SiO_2−WO_3 provided evidence of WO_3 dissolution during the sonochemical deposition of Au nanoparticles. As mentioned above, this data also indicated a loss of Au (in the form of <10 nm nanoparticles) during the etching of Au−SiO_2−WO_3 to form Au−WO_3. The pore diameter of Au−WO_3 was larger than the unetched composite (Au−SiO_2−WO_3), as found for the material not loaded with Au. Overall, Au−SiO_2−WO_3, Au−WO_3, and WO_3 had somewhat larger surface areas than similar materials from the literature; this, with the nanocrystallinity observed by TEM and XRD, made them desirable for adsorption and visible light photocatalysis,[52,53] as will be discussed in the next section.

Adsorption and Photocatalytic Degradation of Methylene Blue. Photocatalysis is widely used in environmental remediation; often the goal in this application is to degrade environmental contaminants under ambient conditions, that is, in aqueous solutions using the solar spectrum. The removal and subsequent photocatalytic degradation of pollutants from aqueous systems has been demonstrated in the presence of semiconducting metal oxides capable of absorbing UV and/or visible light, such as TiO_2 or modified TiO_2. Methylene blue (MB) is a dye that is commonly used to probe the photoactivity of metal oxides, and this molecule was the basis of our own photocatalysis studies using SiO_2−WO_3, WO_3, and the Au nanoparticle-loaded versions of these materials. In this work, we took advantage of the highly negative charges on the WO_3 surface to synthesize an excellent adsorbant for MB. By

DOI: 10.1021/am507806a
ACS Appl. Mater. Interfaces 2015, 7, 1987−1996

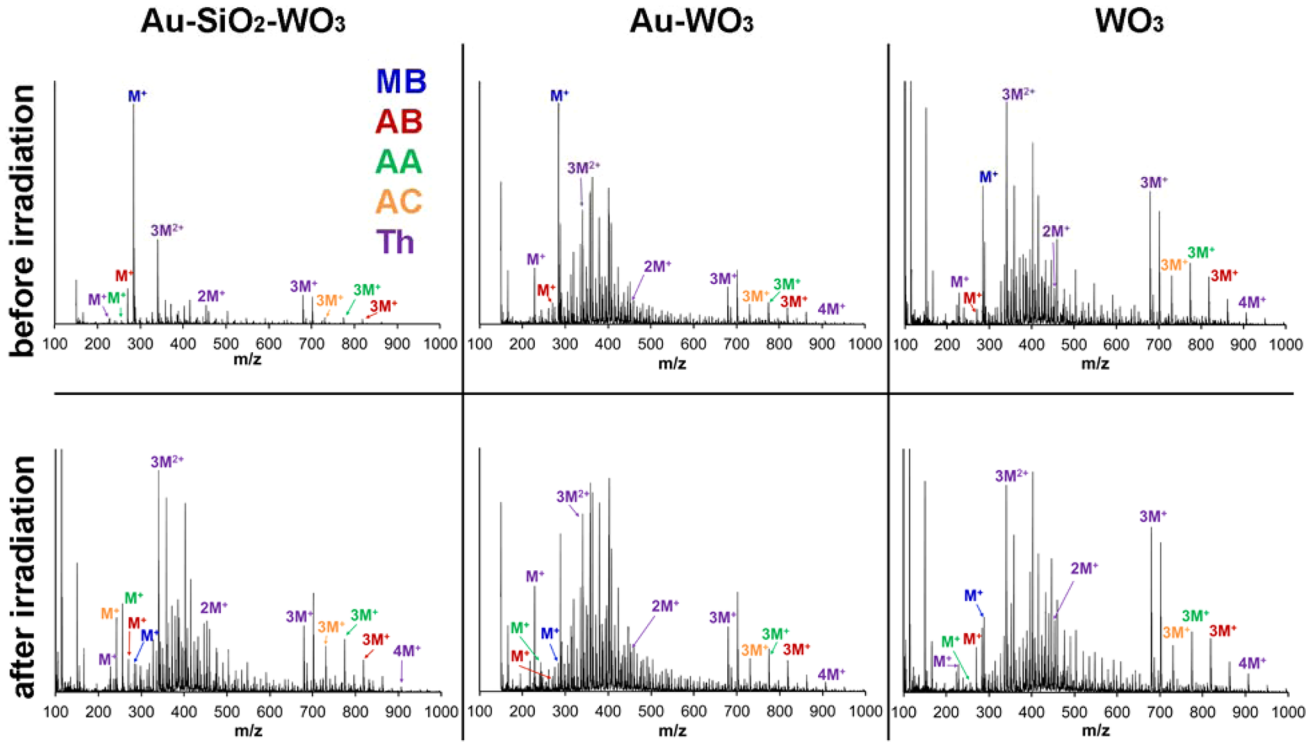

Figure 4. ESI-MS spectra of MB and MB degradation products using Au−SiO_2−WO_3, Au−WO_3, and WO_3 before and after exposure to visible light (300 min). AB, AA, and AC = azure A, B, and C, respectively; Th = thionine. *Y*-axes are in arbitrary intensity units. Note: When present, the highest intensity m/z = 114 peak was truncated so that other peaks can be easily distinguished.

incorporating Au nanoparticles into WO_3-containing catalysts, we also increased the photoactivity of these materials under visible light irradiation.

Photocatalytic experiments were performed by adding materials to an aqueous MB solution, equilibrating the resulting suspensions in the dark for 120 min, and then irradiating the suspensions with visible light for 300 min. A halogen lamp (72 W, 1520 lm) was used for visible light exposures; the UV portion of the spectrum was specifically excluded by passing the light through a UV filter. Electrospray ionization mass spectrometry (ESI-MS) is an effective method to determine byproducts of MB photodegradation in solution[54−56] and this technique was used in our initial experiments to identify degradation products, using Au−SiO_2−WO_3, Au−WO_3, and WO_3. Preliminary analysis of MB by ESI-MS showed a major peak at m/z = 284 due to MB, and a second small peak at m/z = 270 due to contamination with azure B, a monodemethylated product of MB. There were no peaks at higher m/z ratios, indicating that the ESI-MS technique did not cause any further degradation or polymerization of MB.

We found that degradation of MB on our materials proceeded primarily through demethylation (Figure 3) and polymerization, although oxidized products were also observed after irradiation. The addition of MB over 120 min in the dark by Au−SiO_2−WO_3 led to the formation of the fully demethylated product thionine with m/z = 228 (Figure 4), although MB remained the most abundant species. Major MS peaks were also observed at m/z = 340, 358, 402, 453, 680, and 702 due to polymerization of demethylated products.

There are several significant peaks identified throughout the series of mass spectra worth mentioning. The peaks at m/z = 453 and 680 were identified as the thionine dimer and trimer, respectively, which was supported by further analyses of these peaks using tandem MS (MS2, Figure S4, Supporting Information). The +2-charged tetramer of thionine could also be contributing to the peak at m/z = 453 because a small peak at m/z = 906 due to the singly charged thionine tetramer was also observed. The peak at m/z = 340 was identified as the +2-charged thionine trimer from isotope ratio and MS2 analysis. Doubly charged NH_4^+ and 3ACN+2H (ACN = acetonitrile) adducts of the thionine trimer were responsible for the peaks at m/z = 358 and 402, respectively,[57] and the peak at m/z = 702 was due to the Na^+ adduct of the thionine trimer. Other, smaller peaks in the complicated ESI-MS spectrum could be due to several other stable degradation products or adducts of MB and demethylated aggregates at higher m/z values.

During the dark adsorption period, it appeared that MB degradation occurred on the surfaces of Au−SiO_2−WO_3, Au−WO_3, and WO_3 (Figure 4). The ESI-MS data indicated that prior to visible light irradiation, MB remained the major component, but degradation occurred primarily through demethylation to azures A, B, and C and thionine, and polymerization of these products to form dimers and trimers. This correlated with previous reports that used spectrophotometric techniques to characterize MB and thionine polymerization on WO_3 nanocolloids[58] and MB aggregates on amorphous WO_3.[12] Importantly, Au nanoparticles did not affect the types of products observed during adsorption of MB under dark conditions. Also, oxidation of MB was not apparent over Au−SiO_2−WO_3 and WO_3 during this time. However, in the presence of Au−WO_3, a substantial m/z = 319 peak was observed under dark conditions, which could be attributed to the ring-opened MB sulfone. Upon further MS2 analysis, this peak could also be assigned to the Na^+ adduct of an unidentified compound with m/z = 296, which is a potential MB degradation intermediate.

DOI: 10.1021/am507806a
ACS Appl. Mater. Interfaces 2015, 7, 1987−1996

To confirm that crystalline WO_3 was responsible for the extensive polymerization of dye molecules, the pure porous SiO_2 starting material was added to a solution of MB and equilibrated for 120 min under the same conditions. On the basis of ESI-MS data, no significant high m/z peaks are observed, and azure B remains as the secondary peak to MB (Figure S5, Supporting Information). It was clear that SiO_2 did not demethylate MB or aggregate the converted products to any significant extent. Therefore, the addition of acidic WO_3 species to these materials caused extensive demethylation and polymerization of dye molecules to occur during the initial adsorption period. In fact, it has also been observed in different materials that the incorporation of strongly acidic W-sites favors dealkylation and polymerization processes.[59]

After exposure of the catalyst suspensions to visible light for 300 min, the ESI-MS spectra showed significant changes. A more complicated mass spectrum indicated that a wider variety of products was observed as a result of photodegradation. Importantly, similar photocatalyic selectivity was observed over the three studied catalysts, regardless of their composition (Figure 4). Similar to the spectra measured after dark adsorption, MB demethylation products and aggregates of these products remained as the major components, and their abundance at the expense of monomeric MB (small peak at m/z = 284) indicated that MB was almost completely converted. New peaks at m/z = 242 and 256 were attributed to the partial demethylation of MB to form azure C and azure A, respectively. Adducts of partially demethylated products, such as the NH_4^+ adduct of azure B (m/z = 288) were also observed. Major peaks at m/z = 114 and 150 were assigned to stable fragments of MB or demethylated products. Aggregates of thionine, the fully demethylated compound, were still the major products. Continued polymerization of partially demethylated products was shown by the peaks at m/z = 730, 774, and 818, corresponding to the trimers of azure C, azure A, and azure B, respectively. The peak at m/z = 906 was assigned as the thionine tetramer. Similar to the dark equilibration period, Au-loaded and nonloaded materials show similar selectivity toward this photocatalytic reaction.

In addition to demethylation products, the ESI-MS spectra showed evidence of photo-oxidation in the presence of each catalyst. A small peak at m/z = 319 was assigned to the ring-opened sulfone oxidation product of MB during photo-irradiation. However, the sulfoxide (m/z = 303) could not be clearly identified in these tests. Depending on the catalyst, the m/z = 319 peak had varying intensities, with Au–WO_3 showing the most significant peak. It has been accepted that ring sulfur atoms of adsorbed MB are oxidized to the sulfoxide, causing ring opening, and then further oxidized to the sulfone.[52,60] Here, we conclude that demethylation is the primary mode of MB photodegradation, but oxidation may also proceed as a secondary photodegradation pathway. Also, this oxidation pathway may be more facile over Au-loaded catalysts (i.e., Au–WO_3). As highlighted below, Au-loaded catalysts also showed a substantial increase in MB photodegradation activity compared to their nonloaded counterparts. Current experiments are being performed on the interaction of adsorbed MB with the surface, to examine the effect of this strong interaction on the photodegradation process.

After preliminary identification of MB degradation products with ESI-MS, we used UV–visible spectroscopy to quantify the removal of MB over time. A representative series of UV–vis spectra, for Au–SiO_2–WO_3, are shown in Figure 5. The major

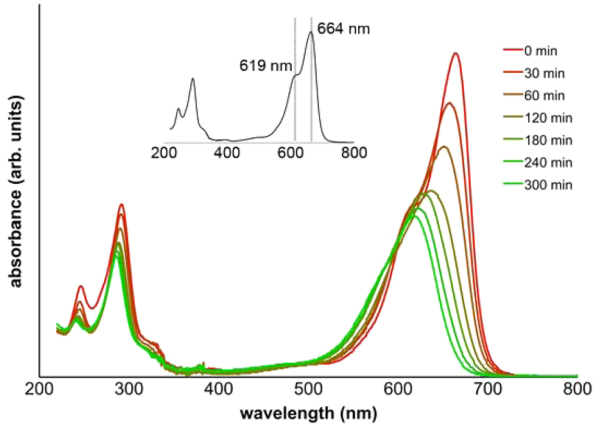

Figure 5. UV–visible spectra of MB in an aqueous solution containing Au–SiO_2–WO_3 during irradiation with visible light. Inset: spectrum of MB in solution (no solid or irradiation).

peak at 664 nm is due to monomeric MB, whereas the shoulder at 619 nm is due to the MB dimer. It is clear that a portion of MB was adsorbed by the solid during the initial period in the dark, and that some of the dimer was adsorbed as well. During the 300 min of visible light irradiation, a hypsochromic shift of the peak at 664 nm was observed due to polymerization and demethylation of MB, which is consistent with the compounds identified by ESI-MS (Figure 4). Similar spectra and hypsochromic shifts were observed in all UV–vis experiments (Figure S6, Supporting Information).

Utilizing the absorbance at 664 nm, we measured the ratios of the remaining MB concentration vs the initial MB concentration (C/C_o) before and during visible light irradiation with each catalyst (Figure 6A). Prior to irradiation, Au–WO_3 and WO_3 both had a significantly greater affinity for MB than Au–SiO_2–WO_3 and SiO_2–WO_3 and were able to adsorb nearly all of the MB from solution. Pure SiO_2 adsorbed an amount of MB (not shown, C/C_o = 0.88) that was comparable to that for Au–SiO_2–WO_3. The large surface area of this sample (~450 m^2/g) accounted for the facile MB adsorption. Visible light irradiation of the MB/catalyst suspension followed the dark equilibration over the course of 300 min. Irradiation of MB in the absence of any porous solid did not produce any change in concentration. Also, there was no MB degradation with Au–SiO_2–WO_3 after 300 min in the dark following the initial adsorption period. This indicated the need for photo-excitation of the catalyst in order for MB degradation to proceed. It is clear from our data that Au–WO_3 and WO_3 behaved similarly, adsorbing most of the MB from solution during the 120 min adsorption period, and converting the remainder during visible light exposure. To compare reaction rates, the photodegradation data was fitted to first-order reaction kinetics, and the observed rate constant (k_{obs}) was calculated as the slope of the linear fit (Figure 6B). Importantly, Au–WO_3 had a faster rate of photodegradation than WO_3 under visible light irradiation. It also appeared that essentially all MB was degraded over Au–WO_3 before 300 min. Thus, it seemed that porous Au–WO_3 was, overall, the best material for total MB removal and degradation. As discussed above, Au–WO_3 did not contain smaller (<10 nm) Au nanoparticles, as they were lost during the etching of Au–SiO_2–WO_3, which could negatively affect the photocatalytic performance of this material. Among the SiO_2-containing materials, Au–SiO_2–WO_3 was slightly better than SiO_2–WO_3 at adsorbing MB, but

DOI: 10.1021/am507806a
ACS Appl. Mater. Interfaces 2015, 7, 1987–1996

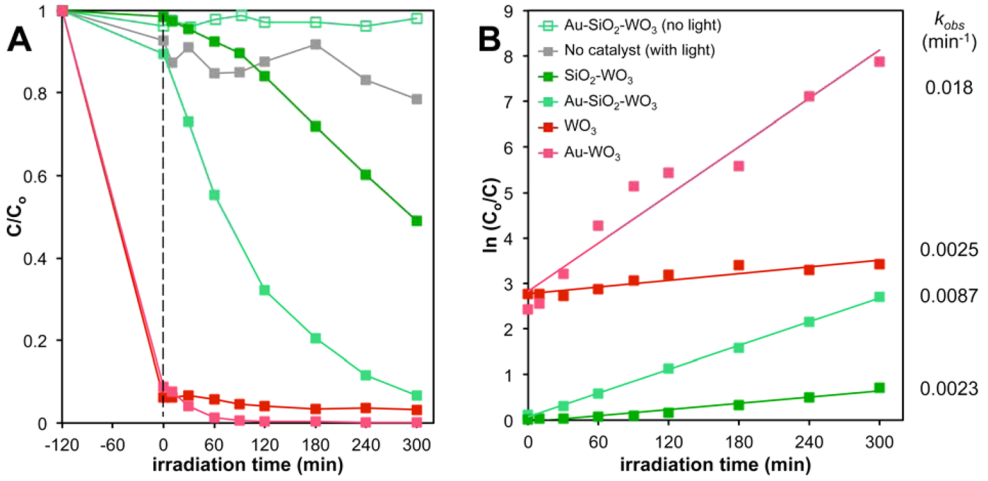

Figure 6. (A) Plot of MB remaining in solution (C/C_o, measured by the absorbance at 664 nm) as a function of photoirradiation time in the presence of various catalysts. The dashed line signifies the start of photoirradiation. (B) First-order reaction kinetics for data shown in panel A; respective k_{obs} are listed to the right of each linear fit. Correlation coefficients (R^2) for each fit in panel B can be found in the Supporting Information, Table S1.

was significantly better at degrading MB during the visible light exposure. Consistent with the pure WO_3 materials, the rate of MB conversion over Au−SiO_2−WO_3 was much greater than SiO_2−WO_3. We attributed this to the presence of small (3−5 nm) Au nanoparticles dispersed throughout the Au−SiO_2−WO_3 catalyst. Almost all of the MB was photocatalytically degraded in the presence of Au−SiO_2−WO_3 (93% conversion), while only 51% conversion was achieved with SiO_2−WO_3 after 300 min. Comparing k_{obs} among the various materials, catalysts not containing SiO_2 showed faster rates of photodegradation than the SiO_2-containing catalysts. The rate of photodegradation was much faster for Au−WO_3 than Au−SiO_2−WO_3, but the difference was not as significant when WO_3 was compared to SiO_2−WO_3. This suggested that the presence of SiO_2 in these materials might hinder the rate of photocatalysis.

Importantly, this more clearly showed the benefit of depositing Au nanoparticles on these catalysts to enhance the rate of photocatalytic degradation of the remaining portion of MB. The improved photocatalytic activity of Au-loaded materials was attributed to the more efficient separation of e^-/h^+ pairs after WO_3 band gap excitation. Upon photoexcitation, the electrons in the WO_3 conduction band (+0.2 eV vs NHE)[61] transfer to Au, which has a lower Fermi level (+0.5 eV vs NHE).[27,62] Photoexcited h^+ can lead to direct oxidative degradation of adsorbed MB, or these excitons can oxidize adsorbed water to create reactive ·OH. The latter mechanism has been proposed by Houas et al.[60] and further accepted by Steiner and Eder[52] for MB photooxidation over mesoporous WO_3. A scheme that relates the proposed photodegradation pathways to the relevant energy levels of the materials involved is shown in Figure S7 (Supporting Information). At this time, other mechanisms for the photocatalytic enhancements due to Au cannot be excluded, however. For instance, nanoparticulate Au deposited on WO_3 catalysts may also benefit from surface plasmon resonance (SPR) that could improve the rate of photocatalysis.[28] In summary, pure WO_3 adsorbed the greatest amount of MB and Au-loaded materials possessed enhanced photocatalytic activity compared to their nonloaded counterparts. Future studies will focus on altering Au loadings to optimize these photocatalysts.

CONCLUSIONS

Porous Au-loaded SiO_2−WO_3 and WO_3 catalysts have been synthesized using a combined sonochemical and nanocasting process. Gold nanoparticles were found to be highly dispersed within the SiO_2 and WO_3 matrices. Also, the size of the deposited Au nanoparticles depended on the substrate composition, and ranged from 3 to 10 nm. Thermally stable Au nanoparticles resisted sintering after repeated high temperature (450 °C) treatments when combined in the SiO_2−WO_3 composite. We have prepared a porous Au−WO_3 photocatalyst simply by etching the Au−SiO_2−WO_3 composite. Mass spectral data in combination with UV−vis spectroscopy confirmed demethylation and polymerization of MB as the major degradation pathways during adsorption and visible light irradiation over Au−SiO_2−WO_3, Au−WO_3, and WO_3. Photooxidation of the MB ring sulfur also occurred as a secondary degradation pathway. The WO_3 contained in these samples was responsible for the extensive polymerization of dye molecules. In addition, samples of pure WO_3 adsorb significantly more MB than SiO_2−WO_3 composites. Finally, we have shown clear photocatalytic benefits in loading SiO_2−WO_3 and WO_3 materials with Au nanoparticles. Gold nanoparticles did not alter the selectivity of MB photodegradation over these catalysts, but the Au-loaded catalysts photocatalytically degraded MB at a greater rate than their nonloaded counterparts. Enhanced exciton (e^-/h^+) separation within Au-loaded catalysts greatly improved the visible light photocatalytic activity of these materials, which may serve as promising environmental remediation photocatalysts.

EXPERIMENTAL SECTION

Materials Characterization. Nitrogen physisorption was carried out at 77 K on a Micromeritics TriStar 3000 surface area and porosity analyzer. Surface areas and pore size distributions were calculated using the BET and BJH methods, respectively. Powder X-ray diffraction (XRD) was performed on a Rigaku MiniFlex II diffractometer using Cu Kα radiation generated with a tube output voltage and current of 30 kV and 15 mA, respectively. The diffractometer was equipped with a water-cooled Scintillator detector that was used at a continuous rate of 0.5° (2θ) per minute. Scanning electron micrographs were recorded with a JEOL JSM-6060 SEM instrument. Dry samples were dispersed on carbon tape and sputter

DOI: 10.1021/am507806a
ACS Appl. Mater. Interfaces 2015, 7, 1987−1996

coated with Au/Pd prior to imaging. Sputter coating was omitted for samples containing Au. Transmission electron micrographs were recorded with a JEOL JEM-1400 TEM instrument operating at 120 kV. In some cases, samples were embedded in Spurrs epoxy resin at 70 °C overnight and then microtomed in order to analyze the interior surfaces of the porous particles. Others were dispersed in ethanol and then dropped onto copper grids. High-resolution transmission electron micrographs were recorded with a JEOL JEM 2100F microscope operating at 200 kV. Samples were dispersed in methyl chloride and transferred to carbon coated copper grids prior to analysis. Energy dispersive X-ray spectroscopy (EDS) elemental analysis of samples was done with an Oxford INCA system attached to the same microscope. Elemental analysis by ICP-OES was completed at Robertson Microlit Laboratories (Ledgewood, NJ). A PerkinElmer Lambda 35 UV/vis spectrometer with PerkinElmer UV Winlab software was used for the measurement of methylene blue in solution. Samples were analyzed in a quartz cuvette with a path length of 1 cm. Electrospray ionization mass spectrometry (ESI-MS) analysis of samples were conducted on an AB Sciex 4000 QTrap (AB Sciex, Framingham, MA) hybrid triple quadrupole/linear ion trap liquid chromatograph-mass spectrometer operating in single quadrupole mode, scanning from 100 to 1000 Da. Positive electrospray ionization (ESI) was used as the ionization source. Source temperature was maintained at 350 °C. Nitrogen was used as the sheath gas (GS1, flow = 30, arbitrary units), auxiliary gas (GS2, flow = 40) and curtain gas (flow = 30). The declustering potential was set to 60. Tandem MS (MS2) spectra were obtained using nitrogen as the collision gas. The accelerating voltage (collision energy) into the collision cell was optimized for each precursor ion to maximize the intensity of product ions. Samples were directly infused at 1 μL/min into an isocratic (50% H_2O and 50% acetonitrile with 0.1% formic acid) mobile phase flow from a Shimadzu Prominence high performance liquid chromatography (HPLC) system (Shimadzu Scientific Instruments, Columbia, MD). Mobile phase flow was maintained at 100 μL/min. Concentrated ammonium hydroxide (29 wt %) was obtained from Fisher Scientific. All other chemicals were obtained from Sigma-Aldrich. All chemicals were used as received.

Synthesis of APMS Mesoporous Template. APMS are disordered mesoporous silica microparticles that can be synthesized very rapidly with good control of porosity and spherical morphology.[63−65] The synthesis of APMS is described in the Supporting Information.

Nanocast Synthesis of Mesoporous WO_3 Microspheres. WO_3 microspheres were created by the method described in the Supporting Information.

Sonochemical Deposition of Au Nanoparticles on SiO_2−WO_3 Spheres. A sonochemical method adapted from Gedanken and co-workers[41] was used to deposit Au nanoparticles on SiO_2−WO_3 spheres at room temperature. In a typical synthesis, 300 mL (16.67 mol) of deionized H_2O was added to a 500 mL round-bottom flask. Then, 0.6 g of SiO_2−WO_3 (APMS previously impregnated twice with ammonium metatungstate, AMT), and 3.088 mL chloroauric acid trihydrate (1 g $HAuCl_4{\cdot}3H_2O$ in 100 mL of H_2O, 15.4 mg of Au, 0.078 mmol Au) were added with stirring. The nominal weight loading of Au was 2.5 wt % based on SiO_2−WO_3. After 30−40 min of stirring, the flask was submerged in a water bath-type sonicator (Branson 2510, 40 kHz, 130 W). During sonication, 19.5 mL of aqueous ammonium hydroxide (14.8 wt %, 8.7 M, 0.170 mol NH_3) was added dropwise in several installments throughout the total sonication time of 45 min. The suspension was then centrifuged for 15 min at 15000*g*, and then the liquid was decanted. The solid was washed twice with deionized water. The damp, yellow-colored solid was dried overnight under vacuum at room temperature. The dry powder was then calcined with the following program: ramp from 298 to 773 K at 0.95 K min^{-1} followed by a 3 h hold at 773 K. The resulting product was a dark wine-colored powder.

Synthesis of Mesoporous Au−WO_3 Microspheres. Au−WO_3 microspheres were created by etching the Au−SiO_2−WO_3 composite material in 10% HF in a similar manner to the SiO_2−WO_3 composite above.

Visible Light Photocatalytic Degradation of Methylene Blue. Photocatalytic methylene blue (MB) degradation experiments were adapted from Steiner and Eder.[52] In a typical experiment, MB in deionized H_2O (50 mL, 4.9 mg MB L^{-1}, 0.015 mM MB) was stirred in a foil-wrapped 100 mL beaker for several minutes. The appropriate photocatalyst powder (0.010 g) was then added and the mixture was left stirring in the dark for 2 h at room temperature to allow for adsorption equilibrium between the dye and the catalyst. After, the mixture was subjected to visible light irradiation (halogen lamp, white light, 72 W, 1520 lm) that was passed through a UV filter (Ru UV filter-001). The light source was positioned approximately 7 cm from the top of the beaker, which was fan-cooled during the experiment. At the appropriate time point, an aliquot was removed from the beaker and passed through a 22 mm syringe filter with a 0.2 μm nylon membrane (VWR International) before analysis by UV−vis spectroscopy and liquid chromatography (LC)-MS. Filtration of the reaction solution was necessary to avoid artificial results due to light scattering from catalyst particles during spectroscopic measurements.

■ ASSOCIATED CONTENT

Supporting Information

Experimental methods used to prepare mesoporous APMS template and nanocast WO_3 microspheres, SEM micrographs and corresponding EDS spectra of spherical WO_3 and Au−WO_3, TEM micrographs of as-prepared Au−SiO_2-WO_3, and Au−SiO_2−WO_3 following calcinations, nitrogen physisorption isotherms and pore size distributions, ESI tandem MS-MS spectra, ESI-MS spectrum of the observed products after 120 min of dark MB adsorption with SiO_2, UV−vis spectra showing adsorption and visible light photodegradation of MB in the presence of SiO_2−WO_3, WO_3, and Au−WO_3, correlation coefficients (R^2) for each first-order linear fit shown in Figure 6B, and proposed photodegradation mechanisms of MB over Au−WO_3 catalysts. This material is available free of charge via the Internet at http://pubs.acs.org.

■ AUTHOR INFORMATION

Corresponding Author

*C. C. Landry. E-mail: christopher.landry@uvm.edu. Fax: +1 802 656 8705.

Notes

The authors declare no competing financial interest.

■ ACKNOWLEDGMENTS

The authors thank the University of Vermont and Spanish MINECO (projects MAT2012-39290-C02-02 and IPT-2012-0574-300000) for financial support, Michele Von Turkovich and Alden M. Clemments for assistance in obtaining TEM images, and David M. Parker for assistance with catalyst synthesis.

■ REFERENCES

(1) Granqvist, C. G. Electrochromic Tungsten Oxide Films: Review of Progress 1993−1998. *Sol. Energy Mater. Sol. Cells* **2000**, *60*, 201−262.

(2) Li, X.-L.; Lou, T.-J.; Sun, X.-M.; Li, Y.-D. Highly Sensitive WO_3 Hollow-Sphere Gas Sensors. *Inorg. Chem.* **2004**, *43*, 5442−5449.

(3) Weinhardt, L.; Blum, M.; Bär, M.; Heske, C.; Cole, B.; Marsen, B.; Miller, E. L. Electronic Surface Level Positions of WO_3 Thin Films for Photoelectrochemical Hydrogen Production. *J. Phys. Chem. C* **2008**, *112*, 3078−3082.

(4) Pokhrel, S.; Simion, C. E.; Teodorescu, V. S.; Barsan, N.; Weimar, U. Synthesis, Mechanism, and Gas-Sensing Application of Surfactant Tailored Tungsten Oxide Nanostructures. *Adv. Funct. Mater.* **2009**, *19*, 1767−1774.

DOI: 10.1021/am507806a
ACS Appl. Mater. Interfaces 2015, 7, 1987−1996

(5) D'Arienzo, M.; Armelao, L.; Mari, C. M.; Polizzi, S.; Ruffo, R.; Scotti, R.; Morazzoni, F. Macroporous WO_3 Thin Films Active in NH_3 Sensing: Role of the Hosted Cr Isolated Centers and Pt Nanoclusters. *J. Am. Chem. Soc.* **2011**, *133*, 5296−5304.
(6) Gondal, M. A.; Seddigi, Z. Laser-Induced Photo-Catalytic Removal of Phenol Using *n*-Type WO_3 Semiconductor Catalyst. *Chem. Phys. Lett.* **2006**, *417*, 124−127.
(7) Sadakane, M.; Tamura, N.; Kanome, N.; Sumiya, S.; Abe, R.; Sano, T. Preparation of Crystalline Tungsten Oxide Nanorods with Enhanced Photocatalytic Activity under Visible Light Irradiation. *Chem. Lett.* **2011**, *40*, 443−445.
(8) Xu, D.; Jiang, T.; Wang, D.; Chen, L.; Zhang, L.; Fu, Z.; Wang, L.; Xie, T. pH-Dependent Assembly of Tungsten Oxide Three-Dimensional Architectures and Their Application in Photocatalysis. *ACS Appl. Mater. Interfaces* **2014**, *6*, 9321−9327.
(9) Zhao, Z. G.; Miyauchi, M. Nanoporous-Walled Tungsten Oxide Nanotubes as Highly Active Visible-Light-Driven Photocatalysts. *Angew. Chem., Int. Ed.* **2008**, *47*, 7051−7055.
(10) Fox, M. A.; Dulay, M. T. Heterogeneous Photocatalysis. *Chem. Rev.* **1993**, *93*, 341−357.
(11) Jeon, S.; Yong, K. Morphology-Controlled Synthesis of Highly Adsorptive Tungsten Oxide Nanostructures and Their Application to Water Treatment. *J. Mater. Chem.* **2010**, *20*, 10146−10151.
(12) Luo, J. Y.; Cao, Z.; Chen, F.; Li, L.; Lin, Y. R.; Liang, B. W.; Zeng, Q. G.; Zhang, M.; He, X.; Li, C. Strong Aggregation Adsorption of Methylene Blue from Water Using Amorphous WO_3 Nanosheets. *Appl. Surf. Sci.* **2013**, *287*, 270−275.
(13) Wang, F.; Li, C.; Yu, J. C. Hexagonal Tungsten Trioxide Nanorods as a Rapid Adsorbent for Methylene Blue. *Sep. Purif. Technol.* **2012**, *91*, 103−107.
(14) Deng, L.; Ding, X.; Zeng, D.; Tian, S.; Li, H.; Xie, C. Visible-Light Activate Mesoporous WO_3 Sensors with Enhanced Formaldehyde-Sensing Property at Room Temperature. *Sens. Actuators, B* **2012**, *163*, 260−266.
(15) Maekawa, T.; Tamaki, J.; Miura, N.; Yamazoe, N. Gold-Loaded Tungsten Oxide Sensor for Detection of Ammonia in Air. *Chem. Lett.* **1992**, *21*, 639−642.
(16) Vallejos, S.; Stoycheva, T.; Umek, P.; Navio, C.; Snyders, R.; Bittencourt, C.; Llobet, E.; Blackman, C.; Moniz, S.; Correig, X. Au Nanoparticle-Functionalised WO_3 Nanoneedles and Their Application in High Sensitivity Gas Sensor Devices. *Chem. Commun.* **2011**, *47*, 565−567.
(17) Kadam, P. M.; Tarwal, N. L.; Shinde, P. S.; Mali, S. S.; Patil, R. S.; Bhosale, A. K.; Deshmukh, H. P.; Patil, P. S. Enhanced Optical Modulation Due to SPR in Gold Nanoparticles Embedded WO_3 Thin Films. *J. Alloys Compd.* **2011**, *509*, 1729−1733.
(18) Naseri, N.; Azimirad, R.; Akhavan, O.; Moshfegh, A. Z. Improved Electrochromical Properties of Sol-Gel WO_3 Thin Films by Doping Gold Nanocrystals. *Thin Solid Films* **2010**, *518*, 2250−2257.
(19) Haruta, M. Size- and Support-Dependency in the Catalysis of Gold. *Catal. Today* **1997**, *36*, 153−166.
(20) Corma, A.; Garcia, H. Supported Gold Nanoparticles as Catalysts for Organic Reactions. *Chem. Soc. Rev.* **2008**, *37*, 2096−2126.
(21) Stratakis, M.; Garcia, H. Catalysis by Supported Gold Nanoparticles: Beyond Aerobic Oxidative Processes. *Chem. Rev.* **2012**, *112*, 4469−4506.
(22) Zhu, H.; Chen, X.; Zheng, Z.; Ke, X.; Jaatinen, E.; Zhao, J.; Guo, C.; Xie, T.; Wang, D. Mechanism of Supported Gold Nanoparticles as Photocatalysts under Ultraviolet and Visible Light Irradiation. *Chem. Commun.* **2009**, 7524−7526.
(23) Primo, A.; Corma, A.; Garcia, H. Titania Supported Gold Nanoparticles as Photocatalyst. *Phys. Chem. Chem. Phys.* **2011**, *13*, 886−910.
(24) Dawson, A.; Kamat, P. V. Semiconductor-Metal Nanocomposites. Photoinduced Fusion and Photocatalysis of Gold-Capped TiO_2 (TiO_2/Gold) Nanoparticles. *J. Phys. Chem. B* **2001**, *105*, 960−966.
(25) Tian, Y.; Tatsuma, T. Mechanisms and Applications of Plasmon-Induced Charge Separation at TiO_2 Films Loaded with Gold Nanoparticles. *J. Am. Chem. Soc.* **2005**, *127*, 7632−7637.
(26) Ismail, A. A.; Bahnemann, D. W.; Bannat, I.; Wark, M. Gold Nanoparticles on Mesoporous Interparticle Networks of Titanium Dioxide Nanocrystals for Enhanced Photonic Efficiencies. *J. Phys. Chem. C* **2009**, *113*, 7429−7435.
(27) Xiang, Q.; Meng, G. F.; Zhao, H. B.; Zhang, Y.; Li, H.; Ma, W. J.; Xu, J. Q. Au Nanoparticle Modified WO_3 Nanorods with their Enhanced Properties for Photocatalysis and Gas-Sensing. *J. Phys. Chem. C* **2010**, *114*, 2049−2055.
(28) Xi, G.; Ye, J.; Ma, Q.; Su, N.; Bai, H.; Wang, C. In Situ Growth of Metal Particles on 3D Urchin-like WO_3 Nanostructures. *J. Am. Chem. Soc.* **2012**, *134*, 6508−6511.
(29) Iliev, V.; Tomova, D.; Rakovsky, S.; Eliyas, A.; Puma, G. L. Enhancement of Photocatalytic Oxidation of Oxalic Acid by Gold Modified WO_3/TiO_2 Photocatalysts under UV and Visible Light Irradiation. *J. Mol. Catal. A: Chem.* **2010**, *327*, 51−57.
(30) Kim, S. W.; Kim, H. K.; Choi, H. W.; Yoo, D. H.; Kim, E. J.; Hahn, S. H. Photocatalytic Activity of Metal-Inserted WO_3 Thin Films Prepared by RF Magnetron Sputtering. *J. Nanosci. Nanotechnol.* **2013**, *13*, 7053−7055.
(31) Abe, R.; Takami, H.; Murakami, N.; Ohtani, B. Pristine Simple Oxides as Visible Light Driven Photocatalysts: Highly Efficient Decomposition of Organic Compounds over Platinum-Loaded Tungsten Oxide. *J. Am. Chem. Soc.* **2008**, *130*, 7780−7781.
(32) Qamar, M.; Yamani, Z. H.; Gondal, M. A.; Alhooshani, K. Synthesis and Comparative Photocatalytic Activity of Pt/WO_3 and Au/WO_3 Nanocomposites under Sunlight-Type Excitation. *Solid State Sci.* **2011**, *13*, 1748−1754.
(33) Tomita, O.; Ohtani, B.; Abe, R. Highly Selective Phenol Production from Benzene on a Platinum-Loaded Tungsten Oxide Photocatalyst with Water and Molecular Oxygen: Selective Oxidation of Water by Holes for Generating Hydroxyl Radical as the Predominant Source of the Hydroxyl Group. *Catal. Sci. Technol.* **2014**, *4*, 3850−3860.
(34) Haruta, M. Catalysis of Gold Nanoparticles Deposited on Metal Oxides. *CATTECH* **2002**, *6*, 102−115.
(35) Parks, G. A. The Isoelectric Points of Solid Oxides, Solid Hydroxides, and Aqueous Hydroxo Complex Systems. *Chem. Rev.* **1965**, *65*, 177−198.
(36) Kosmulski, M. *Chemical Properties of Material Surfaces*; Marcel Dekker: New York, 2001.
(37) Veith, G. M.; Lupini, A. R.; Pennycook, S. J.; Villa, A.; Prati, L.; Dudney, N. J. Magnetron Sputtering of Gold Nanoparticles onto WO_3 and Activated Carbon. *Catal. Today* **2007**, *122*, 248−253.
(38) Navío, C.; Vallejos, S.; Stoycheva, T.; Llobet, E.; Correig, X.; Snyders, R.; Blackman, C.; Umek, P.; Ke, X.; Van Tendeloo, G.; Bittencourt, C. Gold Clusters on WO_3 Nanoneedles Grown via AACVD: XPS and TEM Studies. *Mater. Chem. Phys.* **2012**, *134*, 809−813.
(39) Chen, W.; Cai, W. P.; Liang, C. H.; Zhang, L. D. Synthesis of Gold Nanoparticles Dispersed within Pores of Mesoporous Silica Induced by Ultrasonic Irradiation and its Characterization. *Mater. Res. Bull.* **2001**, *36*, 335−342.
(40) Chen, W.; Cai, W.; Zhang, L.; Wang, G.; Zhang, L. Sonochemical Processes and Formation of Gold Nanoparticles within Pores of Mesoporous Silica. *J. Colloid Interface Sci.* **2001**, *238*, 291−295.
(41) Pol, V. G.; Gedanken, A.; Calderon-Moreno, J. Deposition of Gold Nanoparticles on Silica Spheres: A Sonochemical Approach. *Chem. Mater.* **2003**, *15*, 1111−1118.
(42) Cheng, K.; Sun, W.; Jiang, H.-Y.; Liu, J.; Lin, J. Sonochemical Deposition of Au Nanoparticles on Different Facets-Dominated Anatase TiO_2 Single Crystals and Resulting Photocatalytic Performance. *J. Phys. Chem. C* **2013**, *117*, 14600−14607.
(43) Kneer, E. A.; Raghunath, C.; Raghavan, S.; Jeon, J. S. Electrochemistry of Chemical Vapor Deposited Tungsten Films with

DOI: 10.1021/am507806a
ACS Appl. Mater. Interfaces 2015, 7, 1987−1996

Relevance to Chemical Mechanical Polishing. *J. Electrochem. Soc.* **1996**, *143*, 4095−4100.
(44) Barré, T.; Arurault, L.; Sauvage, F. X. Chemical Behavior of Tungstate Solutions: Part 1. A Spectroscopic Survey of the Species Involved. *Spectrochim. Acta, Part A* **2005**, *61*, 551−557.
(45) Patterson, A. L. The Scherrer Formula for X-ray Particle Size Determination. *Phys. Rev.* **1939**, *56*, 978−982.
(46) Grisel, R. J. H.; Nieuwenhuys, B. E. A Comparative Study of the Oxidation of CO and CH_4 over $Au/MO_x/Al_2O_3$ Catalysts. *Catal. Today* **2001**, *64*, 69−81.
(47) Tsubota, S.; Nakamura, T.; Tanaka, K.; Haruta, M. Effect of Calcination Temperature on the Catalytic Activity of Au Colloids Mechanically Mixed with TiO_2 Powder for CO Oxidation. *Catal. Lett.* **1998**, *56*, 131−135.
(48) Bollinger, M. A.; Vannice, M. A. A Kinetic and DRIFTS Study of Low-Temperature Carbon Monoxide Oxidation over Au-TiO_2 Catalysts. *Appl. Catal., B* **1996**, *8*, 417−443.
(49) Chang, C.-K.; Chen, Y.-J.; Yeh, C.-t. Characterizations of Alumina-Supported Gold with Temperature-Programmed Reduction. *Appl. Catal., A* **1998**, *174*, 13−23.
(50) Rossinyol, E.; Prim, A.; Pellicer, E.; Arbiol, J.; Hernández-Ramírez, F.; Peiró, F.; Cornet, A.; Morante, J. R.; Solovyov, L. A.; Tian, B.; Bo, T.; Zhao, D. Synthesis and Characterization of Chromium-Doped Mesoporous Tungsten Oxide for Gas Sensing Applications. *Adv. Funct. Mater.* **2007**, *17*, 1801−1806.
(51) Qin, Y.; Wang, F.; Shen, W.; Hu, M. Mesoporous Three-Dimensional Network of Crystalline WO_3 Nanowires for Gas Sensing Application. *J. Alloys Compd.* **2012**, *540*, 21−26.
(52) Li, L.; Krissanasaeranee, M.; Pattinson, S. W.; Stefik, M.; Wiesner, U.; Steiner, U.; Eder, D. Enhanced Photocatalytic Properties in Well-Ordered Mesoporous WO_3. *Chem. Commun.* **2010**, *46*, 7620−7622.
(53) Sadakane, M.; Sasaki, K.; Kunioku, H.; Ohtani, B.; Abe, R.; Ueda, W. Preparation of 3-D Ordered Macroporous Tungsten Oxides and Nano-Crystalline Particulate Tungsten Oxides using a Colloidal Crystal Template Method, and their Structural Characterization and Application as Photocatalysts under Visible Light Irradiation. *J. Mater. Chem.* **2010**, *20*, 1811−1818.
(54) Carvalho, H. W. P.; Batista, A. P. L.; Bertholdo, R.; Santilli, C. V.; Pulcinelli, S. H.; Ramalho, T. C. Photocatalyst TiO_2-Co: The Effect of Doping Depth Profile on Methylene Blue Degradation. *J. Mater. Sci.* **2010**, *45*, 5698−5703.
(55) de Souza, W. F.; Guimarães, I. R.; Guerreiro, M. C.; Oliveria, L. C. A. Catalytic Oxidation of Sulfur and Nitrogen Compounds from Diesel Fuel. *Appl. Catal., A* **2009**, *360*, 205−209.
(56) Kertesz, V.; Van Berkel, G. J. Electropolymerization of Methylene Blue Investigated Using On-Line Electrochemistry/Electrospray Mass Spectrometry. *Electroanalysis* **2001**, *13*, 1425−1430.
(57) Huang, N.; Siegel, M. M.; Kruppa, G. H.; Laukien, F. H. Automation of a Fourier Transform Ion Cyclotron Resonance Mass Spectrometer for Acquisition, Analysis, and E-Mailing of High-Resolution Exact-Mass Electrospray Ionization Mass Spectral Data. *J. Am. Soc. Mass Spectrom.* **1999**, *10*, 1166−1173.
(58) Adachi, K.; Mita, T.; Yamate, T.; Yamazaki, S.; Takechi, H.; Watarai, H. Controllable Adsorption and Ideal H-Aggregation Behaviors of Phenothiazine Dyes on the Tungsten Oxide Nanocolloid Surface. *Langmuir* **2010**, *26*, 117−125.
(59) Botella, P.; Solsona, B.; López-Nieto, J. M.; Concepción, P.; Jordá, J. L.; Doménech-Carbó, M. T. Mo-W-Containing Tetragonal Tungsten Bronzes through Isomorphic Substitution of Molybdenum by Tungsten. *Catal. Today* **2010**, *158*, 162−169.
(60) Houas, A.; Lachheb, H.; Ksibi, M.; Elaloui, E.; Guillard, C.; Herrmann, J.-M. Photocatalytic Degradation Pathway of Methylene Blue in Water. *Appl. Catal., B* **2001**, *31*, 145−157.
(61) Mochizuki, D.; Kumagai, K.; Maitani, M. M.; Suzuki, E.; Wada, Y. Precise Control of Photoinduced Electron Transfer in Alternate Layered Nanostructures of Titanium Oxide-Tungsten Oxide. *J. Phys. Chem. C* **2014**, *118*, 22968−22974.
(62) Kamat, P. V.; Shanghavi, B. Interparticle Electron Transfer in Metal/Semiconductor Composites. Picosecond Dynamics of CdS-Capped Gold Nanoclusters. *J. Phys. Chem. B* **1997**, *101*, 7675−7679.
(63) Cheng, K.; El-Boubbou, K.; Landry, C. C. Binding of HIV-1 gp120 Glycoprotein to Silica Nanoparticles Modified with CD4 Glycoprotein and CD4 Peptide Fragments. *ACS Appl. Mater. Interfaces* **2012**, *4*, 235−243.
(64) Gallis, K. W.; Araujo, J. T.; Duff, K. J.; Moore, J. G.; Landry, C. C. The Use of Mesoporous Silica in Liquid Chromatography. *Adv. Mater.* **1999**, *11*, 1452−1455.
(65) Sorensen, A. C.; Fuller, B. L.; Eklund, A. G.; Landry, C. C. Mo-Doped Mesoporous Silica for Thiophene Hydrodesulfurization: Comparison of Materials and Methods. *Chem. Mater.* **2004**, *16*, 2157−2164.

DOI: 10.1021/am507806a
ACS Appl. Mater. Interfaces 2015, 7, 1987−1996